Ocean Modeling with high-order unstructured grid methods

D. B. Haidvogel[1], B.-J. Choi[1], M. Iskandarani[2], J. Levin[1]

[1]*Institute of Marine and Coastal Sciences, Rutgers University*
71 Dudley Road, New Brunswick, NJ 08901 USA
dale@imcs.rutgers.edu, bchoi@imcs.rutgers.edu, julia@imcs.rutgers.edu

[2]*Rosenstiel School of Marine and Atmospheric Science, University of Miami*
4600 Rickenbacker Causeway, Miami, FL 33149, USA
miskandarani@rsmas.miami.edu

ABSTRACT

We review the spatial discretization procedure for three high-order, unstructured grid methods recently developed for use within ocean circulation modeling. They are based respectively on spectral finite element and high-order finite volume formulations. We discuss and contrast the three methods in the context of the shallow water equations.

1 Introduction

Ocean modeling encompasses an enormous range of spatial and temporal scales. One of the great remaining challenges for ocean modeling will be to bridge the scale gaps between global climate processes, basin-scale and regional impacts, and (*e.g.*) ecosystem dynamics on even smaller spatial scales. The geophysical modeling community is exploring several approaches to multiscale simulations in geometrically complex regions, including nested, structured grids; block-structured grids; and unstructured grids. The latter category encompasses finite element and finite volume methods, and their variants. Though historically less prevalent in ocean modeling, these methods are especially attractive because of the geometric flexibility inherent in their unstructured grids. Notably, they allow a single grid of varying cell sizes to address the needs of multiscale simulations.

A promising method with which we have been working is the *spectral element method*. The spectral element method is an *h-p* type finite element method designed to combine the geometrical flexibility of traditional (commonly low-order) finite element methods, and the high-order accuracy normally associated with spectral methods. The spectral element method offers several attractive properties for geophysical simulations: geometrical flexibility with a spatial discretization based on unstructured grids, high-order convergence rates, and dense computations at the elemental level leading to extremely good scalability on parallel computers. Spectral element ocean models based upon the *Continuous Galerkin method* (hereafter, CGM; see below) have been developed by the authors, and have been applied in several idealized dynamical settings. See, for example, Iskandarani et al. (1995), Iskandarani et al. (2003), Curchitser et al. (2001), and Perenne et al. (2000).

Notwithstanding recent progress, a number of computational issues remain unresolved with respect to the application of finite element methods to geophysical flows. These include the enforcement of local conservation properties, the availability of robust advection schemes capable of handling poorly resolved flow features without generating noisy solutions, preservation of water mass properties on decadal and longer time scales, and grid generation and adaptativity.

One possible approach to the resolution of these issues is the use of the *Discontinuous Galerkin Method* (DGM) in conjunction with the spectral finite element discretization. Alternatively, an appropriate high-order *spectral finite volume* (SFV) formulation may be devised. We discuss and illustrate these methods below.

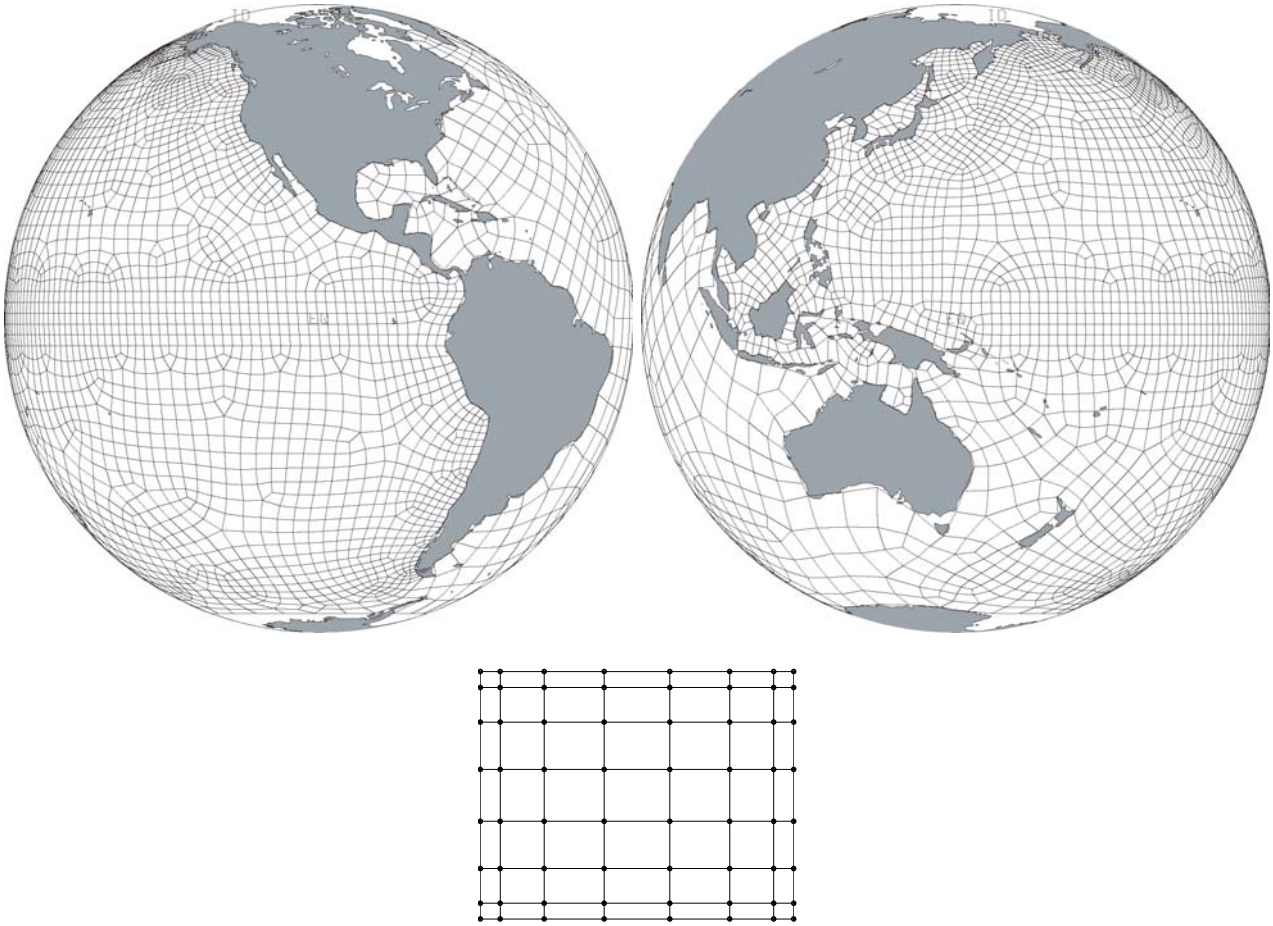

Figure 1: Elemental partition of the global ocean as seen from the eastern and western equatorial Pacific. The inset shows the master element in the computational plane. The location of the interpolation points is marked with a circle, and the structuredness of this local grid is evident from the predictable adjacency pattern between collocation points.

2 A brief overview of the methods

In the solution techniques considered here, the computational domain is divided into a finite number of cells called elements, wherein the solution is approximated with a high-degree polynomial. In the CGM and DGM discretizations, the equations governing the fluid flow are then enforced by minimizing the residual resulting from the approximation. This discretization step turns the partial differential equations into coupled sets of ordinary differential equations that can be integrated in time using a suitable time-integration procedure. This variational (Galerkin) formulation may be replaced by one based upon finite volume considerations, as we describe below for the SFV approach.

Figure 1 shows an example of an elemental grid covering the majority of the global ocean. In these methods, the elements are quadrilaterals. The grid in figure 1 was designed with enhanced resolution in the North Pacific Ocean, and in particular its coastal and equatorial wave guides, essential pathways of El Nino signals. These regions are tiled with small elements of average size of approximately 100 km. The element size increases away from the North Pacific Basin. In particular, the North Atlantic and Indian oceans are tiled at reduced resolution. Thus remote oceanic influences are represented (albeit more crudely) and problems with open boundaries are avoided.

Inside each element the solution is interpolated on a structured grid (Fig. 1). The interpolation points within each element are unevenly spaced and cluster towards the boundary of the element. This special choice of interpolation points serves a dual purpose: eliminating the loss of accuracy that occurs near the edges when

high-order polynomial interpolation is used, and providing the quadrature roots needed to evaluate numerically the integrals arising from the minimization of the residual. The dual roles of interpolation and quadrature translate to tremendous computational efficiency; in particular, it simplifies explicit time-stepping procedures to the level of finite difference techniques.

In the traditional continuous Galerkin approach, the different elements are connected to their immediate neighbors by the requirement that the solution be continuous across the edge they share. The sole restriction is that a single value of the solution be used on either side of the shared edge. Thus, in contrast to higher-order finite difference methods, the halo of points needed to exchange information between elements is limited to those lying on the edge of an element only. This last property makes the spectral element method ideally suited for parallel computations.

The distinguishing feature of the Discontinuous Galerkin Method is that it allows the interpolation of the solution to be discontinuous across element boundaries, and thus takes the localization of the computation a step further than the continuous formulation. Communication between elements takes place via the fluxes exchanged across element boundaries, and these can be biased to favor information coming from the upstream direction. Furthermore, conservation is locally satisfied as fluxes are unique along edges. Thus, the Discontinuous Galerkin Method possesses the two desirable properties of upstream-flux bias and local conservation.

The Spectral Finite Volume method summarized below takes the concept of local conservation to an even higher level. It considers each quadrilateral element to be subdivided futher into a set of $N \times N$ cells, and obtains the discretized equations of motion for each cell by integration over the cell area. Such integration leads to a statement relating the time rate of change of the cell-averaged properties to the fluxes across the cell edges. If these quadratures are carried out at high-order, the resulting approximation is locally conservative (at the cell level) and of high order.

All three of these methods offer a dual path to convergence: algebraic via (global) element refinement, also called *h*-refinement, and exponential (when the solution is suitably smooth) via increasing the order of intra-element interpolation and quadrature (*p*-refinement). Thus they allow the user to control the error either by adjusting the number of elements and their size, and/or by tuning the interpolation order. The optimal allocation of computer resources between the global and local grids ($h-$ versus $p-$type discretization) is problem-dependent. Smooth solutions in regular geometries are computed most efficiently with few elements and high-order interpolation; whereas complicated geometries and localized flow features, such as fronts and jets, call for the use of more elements and lower-order interpolation.

3 The Shallow Water Equations and their Solution

3.1 The shallow water equations (SWE)

The SWE are obtained by vertical integration of the three-dimensional Navier-Stokes equations along with the assumptions of hydrostatic pressure and a vertically uniform horizontal velocity profile. Let Ω be the two-dimensional region occupied by the fluid and let Γ denote its boundary. The reduced gravity SWE in Ω are given by the continuity and momentum equations:

$$\frac{\partial \zeta}{\partial t} + \nabla \cdot [h\mathbf{u}] = 0 \tag{1}$$

$$\frac{\partial \mathbf{u}}{\partial t} + \mathbf{u} \cdot \nabla \mathbf{u} + \mathbf{f} \times \mathbf{u} = \frac{\vec{\tau}}{\rho h} - g' \nabla \zeta - \gamma \mathbf{u} + \frac{\nabla \cdot [\nu h \nabla \mathbf{u}]}{h} \tag{2}$$

where $\mathbf{u} = (u, v)$ is the horizontal velocity vector; $h = H + \zeta$ the fluid thickness; H, the resting depth of the fluid; ζ, the free surface elevation; $\mathbf{f}$, the vertical component of the Coriolis force; $g' = \Delta\rho g/\rho_o$, the reduced gravity; γ, the bottom drag coefficient; ν, the lateral viscosity coefficient; $\vec{\tau} = (\tau_x, \tau_y)$ the wind stress acting on

the surface of the fluid; and, ∇, the two-dimensional gradient operator. A concise discussion of the energetically consistent form of the shallow water equations is given in Gent (1993).

The boundary conditions are Dirichlet conditions on $\mathbf{u}$ and/or ζ:

$$\zeta = \zeta^b \text{ on } \Gamma_D^\zeta, \quad \mathbf{u} = \mathbf{u}^b \text{ on } \Gamma_D \tag{3}$$

and Neumann conditions on $\mathbf{u}$:

$$\nu \nabla \mathbf{u} \cdot \mathbf{n} = \mathbf{q} \text{ on } \Gamma_N \tag{4}$$

where Γ_D and Γ_N are the boundaries where the Dirichlet and Neumann conditions are applied, respectively. Further details on the appropriate boundary conditions are given in Bernardi and Pironneau (1991).

3.2 Galerkin formulations

The starting point of the spectral element ocean model is the Galerkin formulation of the shallow water equations:

$$\int_A \frac{\partial \zeta}{\partial t} w^p \, dA = -\int_A \{\nabla \cdot [h\mathbf{u}]\} \, w^p \, dA \tag{5}$$

$$\int_A \frac{\partial \mathbf{u}}{\partial t} w dA = \int_A \left\{ \frac{\vec{\tau}}{\rho h} - \mathbf{u} \cdot \nabla \mathbf{u} - \mathbf{f} \times \mathbf{u} - g' \nabla \zeta - \gamma \mathbf{u} + \frac{\nu \nabla h \cdot \nabla \mathbf{u}}{h} \right\} w dA - \int_A \nu \nabla \mathbf{u} \cdot \nabla w dA + \int_{\Gamma_N} \mathbf{q} w \, dS \tag{6}$$

where w^p and w are the weight functions associated with the surface elevation and the velocity, respectively.

The spatial discretization proceeds by subdividing the domain into a set of conforming quadrilateral isoparametric elements. Each element is mapped into the unit square in the computational domain (ξ, η), and the variables ζ and $\mathbf{u}$ are interpolated as:

$$\begin{cases} \zeta(\xi,\eta) = \sum_{i=1}^{N^p} \sum_{j=1}^{N^p} \zeta_{i,j}(t) h_i^p(\xi) h_j^p(\eta) \\ \mathbf{u}(\xi,\eta) = \sum_{i=1}^{N^v} \sum_{j=1}^{N^v} \mathbf{u}_{i,j}(t) h_i^v(\xi) h_j^v(\eta) \end{cases} \tag{7}$$

where ζ_{ij} is the surface elevation at the pressure collocation nodes (ξ_i^p, η_{ij}^p), $(i,j) = 1, \cdots, N^p$, and $\mathbf{u}_{ij}$ is the velocity vector at the velocity collocation nodes (ξ_i^v, η_{ij}^v), $(i,j) = 1, \cdots, N^v$. N^p and N^v are the number of nodes per element in the ξ and η directions for the pressure and velocity interpolation, respectively. In order to avoid spurious pressure modes in the incompressible limit, in both the continuous Galerkin and the discontinuous Galerkin formulations, a staggered mesh is employed where the order of the pressure interpolation is two less than the velocity, Iskandarani et al. (1995), therefore $N^p = N^v - 2$ (Figure 2). The spectral finite volume (SFV) formulation differs from the Galerkin spectral element formulation in that it uses an unstaggered grid with $N^p = N^v$; see below.

The basis functions h_i^v for the CGM and DGM formulations are the Legendre cardinal functions, Boyd (2001):

$$h_i^v(\xi) = \frac{-(1-\xi^2) L'_{N^v-1}(\xi)}{N^v(N^v-1) L_{N^v-1}(\xi_i^v)(\xi - \xi_i^v)}, \quad i = 1, 2, \ldots, N^v. \tag{8}$$

L_{N^v-1} denotes the Legendre polynomial of degree $(N^v - 1)$ and L'_{N^v-1} denotes its derivative. The ξ_i^v are the N^v Gauss-Lobatto-Legendre points, *i.e.* they are roots of the function $(1-\xi^2) L'_{N^v-1}(\xi)$. The pressure interpolation functions h_i^p for CGM are defined similarly but with the superscript v replaced by p.

The discontinuous formulation differs from the continuous by the choice of collocation points and basis functions for the pressure, while keeping the velocity definition the same. For the pressure, instead of using a

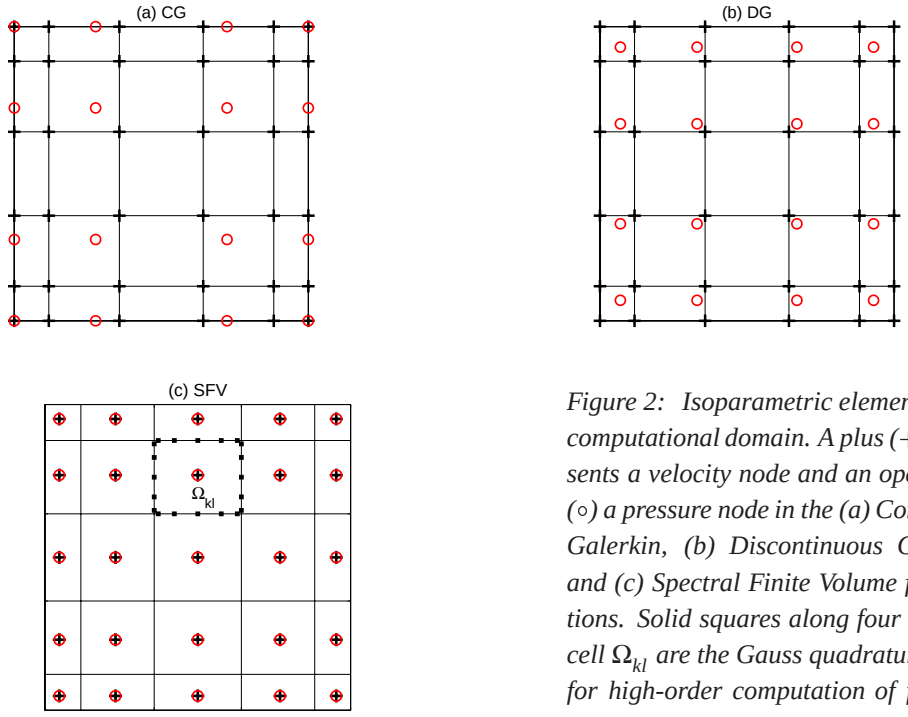

Figure 2: Isoparametric elements in the computational domain. A plus (+) represents a velocity node and an open circle (∘) a pressure node in the (a) Continuous Galerkin, (b) Discontinuous Galerkin, and (c) Spectral Finite Volume formulations. Solid squares along four edges of cell Ω_{kl} are the Gauss quadrature points for high-order computation of fluxes in (c).

Gauss-Lobatto-Legendre grid, a Gauss-Legendre grid is used. The collocation points for the pressure ξ_i^p are the roots of the Legendre polynomial L_{N^p}. The corresponding basis functions are Gauss-Legendre cardinal functions:

$$h_i^p(\xi) = \frac{L_{N^p}(\xi)}{L'_{N^p}(\xi_i^p)(\xi - \xi_i^p)}. \quad i = 1, 2, \ldots, N. \tag{9}$$

Note that point values are collocated at the Gauss-Legendre grid points in the SFV formulation and that the corresponding basis functions, *i.e.*, h_i^v and h_i^p , are the Gauss-Legendre cardinal functions (9).

In the CGM and DGM, a system of ordinary differential equations (for ζ and $\mathbf{u}$) is obtained after inserting (7) into (5) and (6), and substituting $h_i^p h_j^p$ for w^p and $h_i^v h_j^v$ for w:

$$M^p \frac{d\zeta}{dt} = c \tag{10}$$

$$M^v \frac{d\mathbf{u}}{dt} = \mathbf{a}. \tag{11}$$

The matrices M^p and M^v are the mass matrices associated with the pressure and velocity interpolation functions, respectively; they are defined as:

$$M^p_{ij,kl} = \int_A h_i^p(\xi) h_j^p(\eta) h_k^p(\xi) h_l^p(\eta)\, dA \tag{12}$$

$$M^v_{ij,kl} = \int_A h_i^v(\xi) h_j^v(\eta) h_k^v(\xi) h_l^v(\eta)\, dA. \tag{13}$$

In the CGM, the right hand side vectors are:

$$\begin{aligned} \mathbf{a}_{ij} &= \int_A \left\{ \frac{\vec{\tau}}{\rho h} - \mathbf{u}\cdot\nabla\mathbf{u} - \mathbf{f}\times\mathbf{u} - g\nabla\zeta - \gamma\mathbf{u} + \frac{\nu\nabla h\cdot\nabla\mathbf{u}}{h} \right\} h_i^v(\xi) h_j^v(\eta)\, dA \\ &- \int_A \nu\nabla\mathbf{u}\cdot\nabla[h_i^v(\xi) h_j^v(\eta)]\, dA + \int_{\Gamma_N} h_i^v(\xi) h_j^v(\eta)\mathbf{q}\, dS \end{aligned} \tag{14}$$

$$c_{ij} = -\int_A \{\nabla\cdot[h\mathbf{u}]\} h_i^p(\xi) h_j^p(\eta)\, dA. \tag{15}$$

Equations (10) and (11) hold at the elemental level. The assembly procedure adds the contribution of the different elements to the system of equations.

In the DGM formulation, since all the presure collocation points are located inside each element, no continuity of pressure is imposed across element edges. Since ζ is discontinuous, strong forms of the Galerkin formulation of the pressure gradient and horizontal divergence cannot be used; the gradient of the pressure does not exist on the element edges. Instead, a weak form of the two operators is used. For each element E, the weak form of the pressure gradient operator is

$$\int_E g\zeta\nabla w dA - \int_{\delta E} g\zeta \mathbf{n} w dS \quad . \tag{16}$$

The weak form of the horizontal divergence operator is

$$\int_E h\mathbf{u}\cdot\nabla w^p dA - \int_{\delta E} h\mathbf{u}\cdot\mathbf{n} w^p dS \tag{17}$$

where δE is the boundary of an element E, and $\mathbf{n}$ is the normal direction to that boundary.

By the definition of the Gauss-Lobatto Cardinal functions,

$$h_i^v(\xi_j^v) = \delta_{ij},\ \forall i \neq j \tag{18}$$

where δ_{ij} is a Kronecker delta function. Thus the boundary integral in (16) vanishes for all test functions w that correspond to the internal points ($\xi_i^v \neq \pm 1$). For those w that correspond to the edges, the elemental contributions are assembled together. Since approximations of ζ on two neighboring elements are close to each other, we assume that after assembly the boundary integrals from two neighboring elements cancel each other.

The Gauss-Legendre Cardinal functions h^p that are used in the divergence operator (17) have the same property as (18), but there are no collocation points on the edges. All functions h_{ij}^p are not zero on the element edges. Thus the boundary integral does not vanish. There are different ways to compute the numerical flux $(h+\zeta)\mathbf{u}\cdot\mathbf{n}$ on the edge, Cockburn (1998). We choose an upwind numerical flux; an upstream element is used to compute the flux, and then this flux is used in boundary integrals in both neighboring elements.

Replacing the corresponding strong operators in (14) and (15) by the weak operators (16) and (17), we obtain the right hand side vectors for the DGM formulation

$$\begin{aligned}
\mathbf{a}_{ij} &= \int_A \left\{ \frac{\vec{\tau}}{\rho h} - \mathbf{u}\cdot\nabla\mathbf{u} - \mathbf{f}\times\mathbf{u} - \gamma\mathbf{u} + \frac{\nu\nabla h\cdot\nabla\mathbf{u}}{h} \right\} h_i^v(\xi) h_j^v(\eta)\, dA \\
&- \int_A \nu\nabla\mathbf{u}\cdot\nabla[h_i^v(\xi)h_j^v(\eta)]\, dA + \int_A g\zeta\nabla[h_i^v(\xi)h_j^v(\eta)] dA + \int_{\Gamma_N} h_i^v(\xi)h_j^v(\eta)\mathbf{q}\, dS \qquad (19) \\
c_{ij} &= \int_A h\mathbf{u}\cdot\nabla[h_i^p(\xi)h_j^p(\eta)]\, dA - \oint_{\delta A} h^{up}\mathbf{u}\cdot\mathbf{n} h_i^p(\xi)h_j^p(\eta)\, dS, \qquad (20)
\end{aligned}$$

where δA are all the element edges, and $h^{up}\mathbf{u}\cdot\mathbf{n}$ is the upwind flux at the element edge.

Note that even an explicit time integration scheme requires the inversion of the matrices M^v and M^p. Fortunately, the mass matrices can be made diagonal by evaluating the integrals with Gauss-Lobatto quadrature of order N^v, Abramowitz and Stegun (1964), to compute the left hand side in the discretised momentum equations; Gauss-Lobatto and Gauss quadratures of order N^p are used to evaluate the left hand sides in the CGM and DGM forms of the continuity equation, respectively. The diagonal form of the mass matrices leads to tremendous savings in computations and storage with negligible loss of accuracy.

3.3 A spectral finite volume formulation

The finite volume formulation begins by combining equations (1) and (2) into conservative form, Choi et al. (2004). The two-dimensional SWE in Cartesian conservative form are

$$\frac{\partial}{\partial t}h \quad + \quad \frac{\partial}{\partial x}[uh] + \frac{\partial}{\partial y}[vh] = 0$$

$$\begin{aligned}\frac{\partial}{\partial t}[uh] &+ \frac{\partial}{\partial x}[u^2h+\frac{1}{2}g'h^2]+\frac{\partial}{\partial y}[uvh] = fvh+\frac{\tau_x}{\rho}-\gamma uh+\nabla\cdot(\nu h\nabla u) \\ \frac{\partial}{\partial t}[vh] &+ \frac{\partial}{\partial x}[uvh]+\frac{\partial}{\partial y}[v^2h+\frac{1}{2}g'h^2] = -fuh+\frac{\tau_y}{\rho}-\gamma vh+\nabla\cdot(\nu h\nabla v).\end{aligned} \tag{21}$$

This system can now be written more compactly as

$$\frac{\partial \mathbf{U}}{\partial t}+\frac{\partial \mathbf{E}}{\partial x}+\frac{\partial \mathbf{G}}{\partial y} = \mathbf{S} \tag{22}$$

where, **E** and **G** represent the fluxes along the *x*- and *y*-directions, respectively. The vector of unknowns, the Cartesian components of the flux vectors and source terms are

$$\begin{aligned}\mathbf{U} &= \begin{pmatrix} h \\ uh \\ vh \end{pmatrix}, \quad \mathbf{E} = \begin{pmatrix} uh \\ u^2h+\frac{1}{2}g'h^2 \\ uvh \end{pmatrix}, \quad \mathbf{G} = \begin{pmatrix} vh \\ uvh \\ v^2h+\frac{1}{2}g'h^2 \end{pmatrix}, \\ \mathbf{S} &= \begin{pmatrix} 0 \\ fvh+\frac{\tau_x}{\rho}-\gamma uh+\nabla\cdot(\nu h\nabla u) \\ -fuh+\frac{\tau_y}{\rho}-\gamma vh+\nabla\cdot(\nu h\nabla v) \end{pmatrix}.\end{aligned} \tag{23}$$

We stress that the SFV formulation is not based on a variational method, but rather on a finite volume formulation, Alcrudo and Garcia-Navarro (1993). Equation (22) is spatially integrated over a region Ω to obtain the integral form of the equations:

$$\int_\Omega \frac{\partial \mathbf{U}}{\partial t}\,\mathrm{d}\Omega+\oint_\Gamma \mathscr{F}\cdot\mathbf{n}\,\mathrm{d}\Gamma = \int_\Omega \mathbf{S}\,\mathrm{d}\Omega\,, \tag{24}$$

after application of the Gauss theorem. Here $\mathbf{n}$ is the outward unit normal to the boundary Γ of Ω, and $\mathscr{F}\cdot\mathbf{n} = \mathbf{E}n_x+\mathbf{G}n_y$. The first volume integral represents the time rate of change of the amount of $\mathbf{U}$ in Ω, while the surface integral is the total flux of $\mathbf{U}$ through the cell edges. Define $\overline{\mathbf{U}}$ as the average of $\mathbf{U}$ over Ω, *i.e.*,

$$\overline{\mathbf{U}} = \frac{1}{V}\int_\Omega \mathbf{U}\,\mathrm{d}\Omega, \tag{25}$$

where V is the area of Ω in two dimensions and the volume in three dimensions. The finite volume form of the SWE can now be written as:

$$\frac{\mathrm{d}\overline{\mathbf{U}}}{\mathrm{d}t}+\frac{1}{V}\oint_\Gamma \mathscr{F}\cdot\mathbf{n}\mathrm{d}\Gamma = \overline{\mathbf{S}}. \tag{26}$$

Equation (26) is still exact; the numerical approximation comes from evaluating the boundary integral and in time-stepping the area averages.

Each unstructured element is divided into a grid of $N\times N$ cells and is transformed by one-to-one mapping into a computational plane as shown in Figure 2. Each element then contains N^2 cells over which equation (26) will be solved. In order to take advantage of the interpolation properties of spectral methods,Boyd (1994), a point value is interpolated via a high-order Lagrangian interpolant:

$$U(\xi,\eta) = \sum_{i=1}^{N}\sum_{j=1}^{N} U_{ij}h_i(\xi)h_j(\eta) \tag{27}$$

where ξ and η are the coordinates in the computational plane, U_{ij} is the function value at the collocation node of the Gauss-Legendre point $(\overline{\xi}_i,\overline{\eta}_j)$, and $h_i(\xi)$ are the Gauss-Legendre cardinal functions (9).

The cell-averages $\overline{U}_{kl}$ can now be computed by integrating the Lagrangian interpolants over the area of each cell:

$$\overline{U}_{kl} = \sum_{i=1}^{N}\sum_{j=1}^{N} A_{kl,ij}U_{ij}, \quad A_{kl,ij} = \frac{1}{\mathrm{V_{kl}}}\int_{\eta_{l-1}}^{\eta_l}\int_{\xi_{k-1}}^{\xi_k} h_i(\xi)h_j(\eta)|J|\mathrm{d}\xi\mathrm{d}\eta\,. \tag{28}$$

where V_{kl} is the area of cell(k,l), ξ_k and η_l are the Gauss-Lobatto-Legendre points, and $J = (x_\xi y_\eta - x_\eta y_\xi)$ is the Jacobian of the mapping between physical space and computational space. The above operations are a matrix-vector product that maps the N^2 values of U_{ij} into the N^2 cell-averages $\overline{U}_{kl}$. This makes the scheme compact as the reconstruction is now local to each element. A further advantage of this scheme is that it is now possible to uniquely invert the mapping between the function values U_{ij} and the cell averages $\overline{U}_{kl}$ since the averaging matrix A is square. For the given $\overline{U}$ vector of dimension N^2, we reconstruct the N^2 function values $U = A^{-1}\overline{U}$. The matrix A can be computed and stored for each element as a pre-processing step.

A high-order quadrature is used to evaluate the boundary integrals in equation (26). We adopt Gauss quadrature of order N to evaluate these boundary integrals since it provides high accuracy, and does not require flux evaluation at element corners [thus obviating the need to figure out the upwinding directions at these corners, Figure 2(c)]. The discontinuous representation complicates the flux computations near element boundaries where the solution is two-valued. Upwinding along the characteristic direction is required to resolve this discontinuity, and to calculate a unique value for the boundary flux; we use an approximate Riemann solver based on the Harten, Lax, and van Leer Contact (HLLC) flux as described by Toro (1999, 2001).

3.4 Time integration of equations

The explicit time integration of equations (10) and (11) may be performed with (*e.g.*) a third-order Adams-Bashforth (AB3) scheme. Each of the equations in (10) and (11) can be written in the generic form $Mdu/dt = r$ where u and r are the vector of unknowns and the vector of right hand sides, respectively, and M is one of the mass matrices. The AB3 scheme takes the form [see Gear (1971) for example]:

$$u^{n+1} = u^n + \Delta t M^{-1}\left[\frac{23}{12}r^n - \frac{16}{12}r^{n-1} + \frac{5}{12}r^{n-2}\right]. \tag{29}$$

The calculations require information at two previous time levels and thus a start-up method is needed at the initial timestep; we choose a fourth-order Runge-Kutta scheme. All computations are performed at the elemental level and only the vector r needs to be assembled at each timestep. As an alternative to (29), a third-order Runge-Kutta method might also be used, Choi et al. (2004).

4 Supercritical channel flow

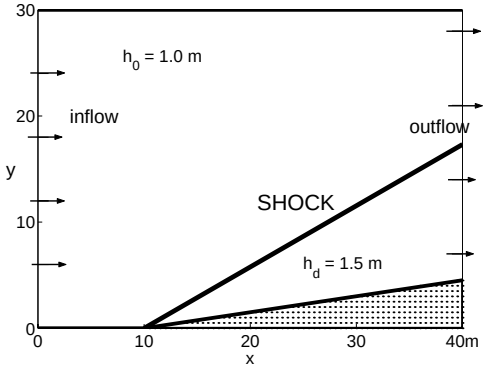

Figure 3: Schematic diagram of oblique shock front in the supercritical channel flow.

We briefly illustrate the results of these methods with the example of supercritical flow in a constricted channel. Additional test problems and convergemce studies are described in Choi et al. (2004) and Iskandarani et al. (2004).

When a supercritical flow encounters a sudden change in channel cross-section, through a boundary wall constriction on one side wall of a channel as depicted in Figure 3, an oblique hydraulic jump (discontinuity)

K	CG			DG			SFV		
	Grid	h	$\|\mathbf{u}\|$	Grid	h	$\|\mathbf{u}\|$	Grid	h	$\|\mathbf{u}\|$
4×3	21×16	1.396	8.243	21×16	1.351	8.295	24×18	1.486	7.961
8×6	41×31	1.450	7.633	41×31	1.432	8.130	48×36	1.491	7.959
12×9	61×46	1.535	8.577	61×46	1.455	8.060	72×54	1.495	7.956
16×12	81×61	1.450	7.259	81×61	1.463	8.011	96×72	1.496	7.955
exact		1.500	7.956		1.500	7.956		1.500	7.956

Table 1: Comparison of metrics for the supercritical flow test problem obtained on grids of various resolution (h-refinement). For CGM and DGM, the velocity grid has $N = 6$ collocation points, and the pressure grid has $N = 4$ collocation points. Both the velocity and pressure grids have $N = 6$ collocation points for the SFV method. K is the number of elements. "Grid" specifies the number of velocity collocation points; $|\mathbf{u}|$ (m/s), the average value of flow speed behind the shock; and h, the average value of the water depth behind the shock.

originates at the constriction. The initial conditions over the entire domain including the inlet at $x = 0$ are h_0 = 1.0 m, u_0 = 8.57 m/s, and v_0 = 0 m/s; this corresponds to Fr = 2.74 at the inflow boundary. The rest of the boundary conditions are supercritical outflow at x = 40 m and no-normal flow along the side walls. No boundary conditions are required on the outflow boundary since the flow is supercritical. For a constriction angle of 8.95°, the analytical solution is ζ = 0.5 m, $|\mathbf{u}| = \sqrt{u^2 + v^2}$ = 7.956 m/s, and Fr = 2.075 downstream of the jump; the angle between the original flow direction and the jump is 30°.

Table 1 compares the performance of the three methods described above. Note that upon grid refinement, both DGM and the SFV methods approach the exact solution, whereas the continuous treatment shows little convergence. This reflects the slightly dissipative nature of the DGM and SFV algorithms. By contrast, the CGM model is essentially inviscid, and therefore suffers from Gibbs oscillations irrespective of grid resolution.

5 Three-dimensional considerations

The representation of the vertical structure of the water column is particularly problematic as it involves complicated (tall and steep) marine topography covering a wide range of length scales. Three common choices of vertical coordinate are: 1) z-level, where the vertical is represented by a stack of horizontal slabs interrupted by topography; 2) terrain-following coordinates, where the computational surfaces follow the sloping bathymetry; and 3) layered models, where the water column is divided into isopycnal (equal density) layers. For a spectral element model, the z-level approach is a poor choice; the first-order representation of the topography is inconsistent with the high-order algorithms.

Terrain-following discretizations have the virtue of representing topographic processes accurately provided the underlying bathymetry is well resolved on the computational mesh. Since it is in this limit that these higher-order methods best apply, terrain-following coordinates are an obvious choice for geophysical spectral element methods. In particular, the vertical discretization of a fully three-dimensional spectral element ocean model (SEOM) is based on a spectral element formulation wherein the elements are three-dimensional hexahedra that follow the bottom topography, Iskandarani et al. (2003). A three-dimensional spectral element grid can thus be produced by stacking vertically and conformally a number of two-dimensional grids. Note, in particular, that vertical resolution may still be distributed according to *a priori* considerations.

The layered discretization has until recently been impractical as it requires robust numerical schemes that can handle discontinuous solutions without noise generation. The arrival of the DGM and SFV methods suggests that layered treatments may now be feasible. This is an area of active research.

Acknowledgements

The development and application of the spectral element model has been supported by grants from the Office of Naval Research (Ocean Modeling and Prediction) and the National Science Foundation (Advanced Computational Methods, Physical Oceanography).

References

Abramowitz, M., Stegun, I., June 1964. Handbook of Mathematical Functions, 1st Edition. Vol. 55 of Applied Mathematics Series. National Bureau of Standards, Washington, DC.

Alcrudo, F., Garcia-Navarro, P., 1993. A high-resolution Godunov-type scheme in finite volumes for the 2D Shallow-Water equations. Int. J. Numer. Methods Fluids 16, 489–505.

Bernardi, C., Pironneau, O., 1991. On the shallow water equations at low Reynolds numbers. Communications in Partial Differential Equations 16 (1), 59–104.

Boyd, J. P., 1994. Hyperviscous shock layers and diffusion zones: Monotonicity, spectral viscosity, and pseudospectral methods for very high order differential equations. Journal of Scientific Computing 9, 81–106.

Boyd, J. P., 2001. Chebyshev and Fourier Spectral Methods, 2nd Edition. Dover Publications, Mineola, NY.

Choi, B.-J., Iskandarani, M., Levin, J., Haidvogel, D. B., 2004. A spectral finite-volume method for the shallow water equations. Monthly Weather Review 132, 1777–1791.

Cockburn, B., 1998. An introduction to the discontinuous Galerkin methods for convection dominated flows. In: Advanced Numerical Approximation of Nonlinear Hyperbolic Equations. Springer-Verlag, pp. 151–268.

Curchitser, E. N., Haidvogel, D., Iskandarani, M., 2001. On the transient adjustment of a mid-latitude abyssal ocean basin with realistic geometry and bathymetry. Journal of Physical Oceanography 31, 725–745.

Gear, C. W., 1971. Numerical Initial Value Problems in Ordinary Differential Equations. Prentice-Hall, Engelwood-Cliffs, NJ.

Gent, P., May 1993. The energetically consistent Shallow-Water equations. Journal of the Atmospheric Sciences 50 (9), 1323–1325.

Iskandarani, M., Haidvogel, D. B., Boyd, J., 1995. A staggered spectral finite element model for the shallow water equations. International Journal for Numerical Methods in Fluids 20, 393–414.

Iskandarani, M., Haidvogel, D. B., Levin, J. G., 2003. A three-dimentional spectral element model for solution of the hydrostatic primitive equations. Journal of Computational Physics 186, 397–425.

Iskandarani, M., Levin, J., Choi, B.-J., Haidvogel, D. B., 2004. Comparison of advection schemes for high order h-p finite element and finite volume methods. Ocean Modelling, accepted.

Perenne, N., Haidvogel, D. B., Boyer, D., 2000. Laboratory-numerical model comparisons of flow over a coastal canyon. Journal of Atmospheric and Oceanographic Technology 18, 235–255.

Toro, E. F., 1999. Riemann Solvers and Numerical Methods for Fluid Dynamics. Springer-Verlag.

Toro, E. F., 2001. Shock-Capturing Methods for Free-Surface Shallow Flows. John Wiley and Sons.